Proceedings of the 28th IEEE
EMBS Annual International Conference
New York City, USA, Aug 30-Sept 3, 2006

UWB Microwave Breast Cancer Detection: Generalized Models and Performance Prediction

Yifan Chen[1], Erry Gunawan[1], Yongmin Kim[2], Kay Soon Low[1], Cheong Boon Soh[1], and Lin Lin Thi[1]

[1]Biomedical Engineering Research Centre, Nanyang Technological University, Singapore
[2]Department of Bioengineering, University of Washington, Seattle, WA 98195, USA

Abstract — **This paper presents a generic framework for the modeling of ultra-wideband (UWB) signal propagation in human breast, which facilitates system-level simulations and provides performance prediction. The clutter associated with the breast tissue heterogeneity is modeled through several key parameters depending on the tissue compositions. Subsequently, important channel properties such as the backscatter energy and the probability density function of time-of-arrival are derived. The modified Hermite polynomials, which fit well into the real pulse shapes, are then used to model the UWB signals. Armed with the channel/signal model preliminaries, three metrics are proposed, namely, the mean clutter response, the clean tumor response, and the worst-case clutter response. The generalized model provides a parsimonious way to study the effects of tissue structures, pulse templates, and array setup on the performance of a specified UWB imaging system. Numerical examples are used to demonstrate the usefulness of the proposed approach.**

Index Terms — **UWB microwave imaging, statistical clutter modeling, pulse shapes, breast cancer detection.**

I. Introduction

In recent years, high-resolution ultra-wideband (UWB) based microwave imaging has been investigated in the detection of early breast cancer [1]-[5]. Preliminary results have been obtained with near-field tomographic image reconstruction (TIR) [1], confocal microwave imaging [2], space-time beamforming [3], generalized likelihood ratio test based detection [4], and time-of-arrival (TOA) data fusion method [5]. On the one hand, the TIR attempts to reproduce the wavenumber variations in the object of interest. However, as the algorithms generally pose an ill-conditioned inverse scattering problem, errors in the measured data may be amplified. On the other hand, UWB radar based techniques are simpler and computationally less expensive. However, estimates of material properties are not directly provided, rather areas of strong backscatter energy are indicated.

Till now, the tumor detection capabilities of various imaging techniques are evaluated through finite-difference time-domain (FDTD) methods [2]-[4]. As an FDTD simulation does not enable a simple mapping of tissue compositions, UWB pulse shape, and array setup to the performance metrics (e.g., signal-to-clutter ratio), discovery of new imaging systems has to rely on individual intuition and heuristic inspection of the scattering process. In this paper, we provide a *parsimonious* solution to bridge the gap between the channel/signal structures and the detection capability. First, in a random propagation medium such as human breast, the wavenumber varies from point to point. In most cases, it would be unnecessary to describe their values at all locations and at all times. Therefore, we characterize the medium statistically and seek *average* information about the behavior of the wave in it. Next, as a candidate model for the UWB signals, the modified Hermite polynomials (MHPs) are used to study the effect of pulse shapes on the microwave imaging qualities. Finally, the concepts of mean clutter response (MCR), clean tumor response (CTR), and worst-case clutter response (WCR) are introduced to assess the feasibility of a specified UWB microwave imaging system.

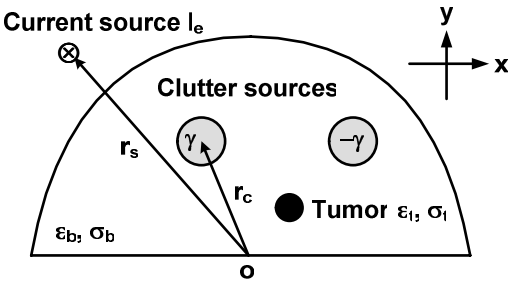

Fig. 1. A canonical 2-D breast phantom with uniformly distributed clutter sources generated by tissue heterogeneity and a piece of tumor tissue.

The paper is organized as follows. In Section II, the details of the channel and signal modeling methodologies are presented, followed by derivation of the three performance measures. In Section III, numerical examples are used to illustrate the usefulness of the proposed approach. Finally, some concluding remarks are drawn in Section IV.

II. Modeling Methodologies

A. Canonical Breast Model

In this initial investigation, a two-dimensional (2-D) model is considered for which all material structures are assumed to be infinitely long. The various tissues are considered non-dispersive, and the skin layer is omitted by assuming that reflections from the skin-breast interface have been removed by applying an artifact removal algorithm [3]. The antennas are immersed in a low-loss material with dielectric property matching the average breast permittivity [2]-[5].

The canonical breast phantom is a dielectric semi-cylinder centered at the origin as illustrated in Fig. 1. The clutter

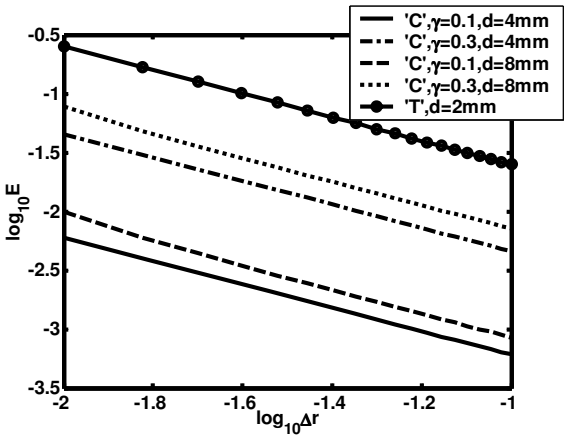

Fig. 2. Backscatter energy versus the propagation distance.

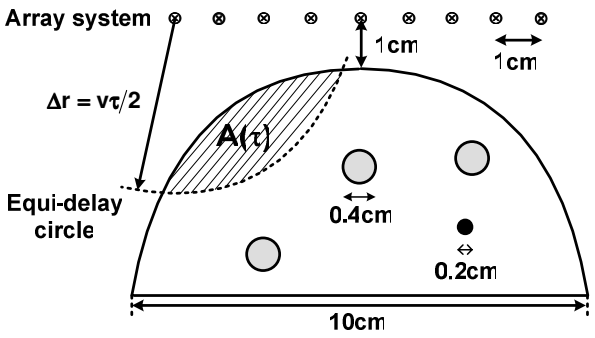

Fig. 3. Illustration of calculation of the pdf of TOA and the array setup for the numerical examples.

sources associated with tissue heterogeneity are infinite-length dielectric cylinders and uniformly distributed within the breast. The dielectric constant and conductivity of the average breast tissue are ε_b and σ_b, and these values for the clutter sources are $(1 \pm \gamma)\varepsilon_b$ and $(1 \pm \gamma)\sigma_b$, respectively. The symbol γ denotes the mean percentage variation about the average value. We further assume that it is equally probable for a clutter source to have either $+\gamma$ or $-\gamma$ variation. Mammary glands and ducts can also be taken into account by uniformly positioning a group of cylinders having a higher percentage variation $+\gamma'$.

The tumor tissue is then modeled as a small cylinder and is directly interposed in the breast phantom.

B. Backscatter Energy and Probability Density Function (pdf) of Backscatter Pulse Time-of-Arrival

To compute the backscatter energy E, we consider a clutter source centered at $\mathbf{r_c}$, oriented parallel to an electric current line source I_e located at $\mathbf{r_s}$ as shown in Fig. 1. The analytical expression for the backscatter field at $\mathbf{r_s}$ is [4]:

$$G(\mathbf{r_c}, \mathbf{r_s}, \omega) = \frac{\omega \mu_0 I_e}{4} \sum_{\nu=-\infty}^{+\infty} \alpha_\nu H_\nu^{(2)}(k_b \Delta r)$$

$$\text{where } \alpha_\nu = \frac{J_\nu'(z_b) J_\nu(z_c) - \sqrt{1 \pm \gamma} J_\nu(z_b) J_\nu'(z_c)}{\sqrt{1 \pm \gamma} H_\nu^{(2)}(z_b) J_\nu'(z_c) - H_\nu^{(2)\prime}(z_b) J_\nu(z_c)} \quad (1)$$

where ω is the frequency, μ_0 is the permeability of free space, and $\Delta r = |\mathbf{r_c} - \mathbf{r_s}|$. $H_\nu^{(2)}$ denotes the νth-order Hankel function of the second kind, and J_ν denotes the νth-order Bessel function. The prime ($'$) represents a derivative with respect to the argument of the function. $z_b = k_b d/2$ and $z_c = k_c d/2$ where d is the diameter of the clutter source, and k_b and k_c are the wavenumbers for the breast tissue and the clutter source, respectively. It is further assumed that the excitation of the sensor is a modulated Gaussian UWB pulse:

$$I_e(t) = I_0 \sin\left[\omega(t - t_0)\right] \exp\left[-\frac{(t - t_0)^2}{2T^2}\right] \quad (2)$$

where ω = 6 GHz, T = 0.035 ns, and t_0 = 0.2 ns. The received signal is calculated from (1) and (2) by performing an inverse discrete Fourier transform for a set of frequencies spanning 1-11 GHz, and the backscatter energy E can be obtained.

Fig. 2 depicts the relationship between E and Δr. The average values of the dielectric properties of breast tissue are ε_b = 21.50 and conductivity σ_b = 1.66 S/m, corresponding to the numerical breast phantoms 'n4' ~ 'n8' used in [4]. 'C' represents a clutter source and 'T' represents a malignant tumor with the dielectric properties ε_t = 50.73 and σ_t = 4.82 S/m. As shown in Fig. 2, $\log_{10}E$ scales linearly with $\log_{10}\Delta r$:

$$\log_{10} E = K(\gamma, d) - n \log_{10} \Delta r \quad (3)$$

K is the scattering cross section, which is a function of the dielectric properties and diameter of the scattering medium. The path loss exponent n takes into account the radial spreading effect of the spherical waves. n = 1 for 2-D propagation. Note that in a real breast phantom, double and multiple scatterings will cause attenuation and absorption along the path, thus a larger value of n is expected.

The next step is to derive the pdf of TOA for backscatter pulses. For monostatic radar configurations, the clutter sources that introduce the same delay τ would lie on a circle of radius $\Delta r = v\tau/2$ centered at the transmit/receive element, where v is the speed of electromagnetic waves in the surrounding medium (see also Fig. 3). Let us consider the shaded area $A(\tau)$, formed by the equi-delay circle and the boundary line of the breast. Since the clutter sources are uniformly distributed within the breast, it is apparent that the shaded area is proportional to the cumulative distribution function (cdf) of the TOA, $F_\tau(\tau)$, i.e.,

$$F_\tau(\tau) = A(\tau)/A_b = 8A(\tau)/(\pi D^2) \quad (4)$$

where A_b is the cross-sectional area of the breast and D is the diameter of the breast phantom. Subsequently, the pdf of TOA is obtained as the derivative of $F_\tau(\tau)$ with respect to τ.

C. Generalized Signal Models

A key step in the development of a generic framework is to propose representative models for the UWB signal. The model should offer the following desired properties:

– The pulses have zero dc component.

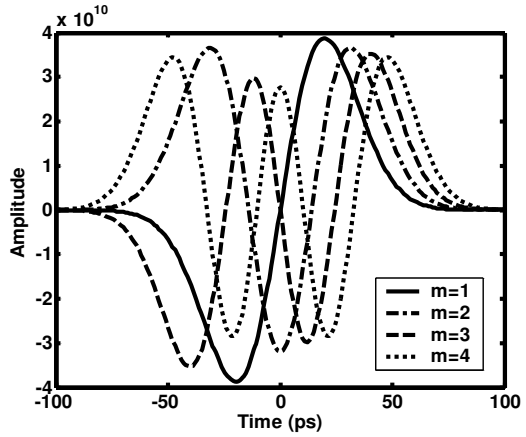

Fig. 4. Time response of the MHP of orders m = 1, 2, 3, 4 normalized to unit energy. The number of zero crossing is equal to m.

– The pulse duration and bandwidth can be easily controlled.
– The pulse shapes can fit well into the commonly used UWB waveforms (e.g., Gaussian monocycle or doublet).
– Different members of the pulse family can represent the significant shaping in the radiation, propagation, and reception processes (e.g., various order differentiation) [6].

In this paper, we suggest the MHP [7] as an appropriate family of waveforms for the quantitative study:

$$h_m(t) = (-1)^m \exp\left(\frac{t^2}{4T^2}\right)\frac{d^m}{dt^m}\left\{\exp\left(-\frac{t^2}{2T^2}\right)\right\} \quad (5)$$

where m = 0, 1, 2, ·· is the order of the MHPs and $-\infty < t < +\infty$. T controls the duration of the pulses. Fig. 4 shows the time-domain representations of the MHPs for T = 14 ps. The time functions are normalized to unit energy, and it can be shown that the normalization constant is $1\Big/\left(T\sqrt{m!\sqrt{2\pi}}\right)$. An arbitrary phase shifted sinusoid can be used to modulate the MHP in order to gain more flexibility in the frequency domain, which is defined as follows [7]:

$$\tilde{h}_m(t) = h_m(t)\sin(\omega t + \varphi_r) \quad (6)$$

where φ_r is an arbitrary phase that can be zero without loss of generality. Note that (6) reduces to the modulated Gaussian function as shown in (2) for m = 0 and φ_r = 0.

D. Performance Metrics

Consider a generic system, which constructs the image by synthetically focusing the processed signal at a specific point $\mathbf{r_c}$ in the breast. The intensity value at $\mathbf{r_c}$ can be represented as:

$$P(\mathbf{r_c}) = \sum_{i=1}^{I} \mathbb{M}_{i,\mathbf{r_c}}\left[\sum_{n=1}^{N}\left(\kappa_{i,n}\sqrt{E_{i,n}}h_{i,n}\left(t-\tau_{i,n}\right)\right)\right] \quad (7)$$

where I and N are the numbers of antenna elements and scattering centers (including clutter sources and the tumor), respectively. $\kappa_{i,n} \in \{\pm 1\}$ depending on whether the dielectric property variation is positive or negative. $E_{i,n}$ and $h_{i,n}$ are the backscatter energy and the pulse shape corresponding to the ith antenna element and the nth scattering center, respectively. $\tau_{i,n}$ is the propagation delay. $\mathbb{M}_{i,\mathbf{r_c}}[\cdot]$ is a general mapping function, which maps the signal received at the ith sensor to a quantifiable value indicating the scattering strength at $\mathbf{r_c}$. $\mathbb{M}_{i,\mathbf{r_c}}[\cdot]$ usually consists of a two-stage operation. In Stage I, distances from each antenna to a hypothetical focal point are computed and converted into time delays. The receive signals are then delayed to align the return from the hypothetical point. In Stage II, the time-shifted signals are processed to obtain an intensity measure based on the pulse characteristics.

Without much loss of generality, the following mapping function is considered for the quantitative analysis:

$$P(\mathbf{r_c}) = \sum_{i=1}^{I}\int_{\Xi_i}\left\{\sum_{n=1}^{N}\left[\kappa_{i,n}\sqrt{E_{i,n}}h_{i,n}\left(t-\tau_{i,n}+\tilde{\tau}_i(\mathbf{r_c})\right)\right]\right\}^2 dt \quad (8)$$

where $\tilde{\tau}_i(\mathbf{r_c}) = 2|\mathbf{r_c}-\mathbf{r_{s,}}_i|/v$ with $\mathbf{r_{s,}}_i$ being the location of sensor i. Ξ_i is the integration window during the energy detection stage (Stage II). To study the average detection capability of the system, we take the expectation of both sides of (8):

$$\begin{aligned}\mathbb{E}\left[P(\mathbf{r_c})\right] &= \sum_{i=1}^{I}\sum_{n=1}^{N}\mathbb{E}\left\{\int_{\Xi_i}E_{i,n}h_{i,n}^2\left(t-\tau_{i,n}+\tilde{\tau}_i(\mathbf{r_c})\right)dt\right\}\\ &+\sum_{i=1}^{I}\sum_{\substack{n_1\\ n_1\neq n_2}}\sum_{n_2}\mathbb{E}\left\{\int_{\Xi_i}\kappa_{i,n_1}\kappa_{i,n_2}\sqrt{E_{i,n_1}E_{i,n_2}}h_{i,n_1}\left(t-\tau_{i,n_1}+\tilde{\tau}_i(\mathbf{r_c})\right)\right.\\ &\left.\times h_{i,n_2}\left(t-\tau_{i,n_2}+\tilde{\tau}_i(\mathbf{r_c})\right)dt\right\}\end{aligned} \quad (9)$$

where $\mathbb{E}\{\cdot\}$ is the expectation operator. Since it is equally probable for κ to be +1 or -1, the second term of (9) would approach to 0. Consequently, by separating the clutter response from the tumor response, (9) can be rewritten as:

$$\begin{aligned}\mathbb{E}\left[P(\mathbf{r_c})\right] &= \sum_{i=1}^{I}\sum_{n=1}^{N}\mathbb{E}\left\{\int_{\Xi_i}E_{i,n}h_{i,n}^2\left(t-\tau_{i,n}+\tilde{\tau}(\mathbf{r_c})\right)dt\right\}\\ &= \underbrace{\sum_{i=1}^{I}\left\{(N-1)\int_{\Omega_i}\int_{\Xi_i}E(\tau)h^2\left(t-\tau+\tilde{\tau}(\mathbf{r_c})\right)f_i(\tau)\,dt\,d\tau\right\}}_{\text{Mean clutter response}}\\ &+\underbrace{\sum_{i=1}^{I}\int_{\Xi_i}E_{i,n_t}h_{i,n_t}^2\left(t-\tau_{i,n_t}+\tilde{\tau}(\mathbf{r_c})\right)dt}_{\text{Clean tumor response}}\end{aligned} \quad (10)$$

where $f_i(\tau)$ is the pdf of TOA at sensor i and Ω_i is the integration region in the τ-domain. The subscript n_t denotes the delay, energy, and shape of the pulse backscattered by the tumor. The first term of (10) characterizes the MCR, which determines the clutter response in an average manner. The second term of (10) is defined as the CTR, which corresponds to the tumor response in the absence of clutter interference. Note that (10) implies identically and independently distributed (i.i.d.) clutter sources.

We further define the WCR as the clutter response when all the backscatter pulses have the same path delay $\tilde{\tau}_i(\mathbf{r_c})$, i.e., $\tau_{i,n} \equiv \tilde{\tau}_i(\mathbf{r_c})$, $\forall n \neq n_t$. Following from (10), the WCR can be calculated as:

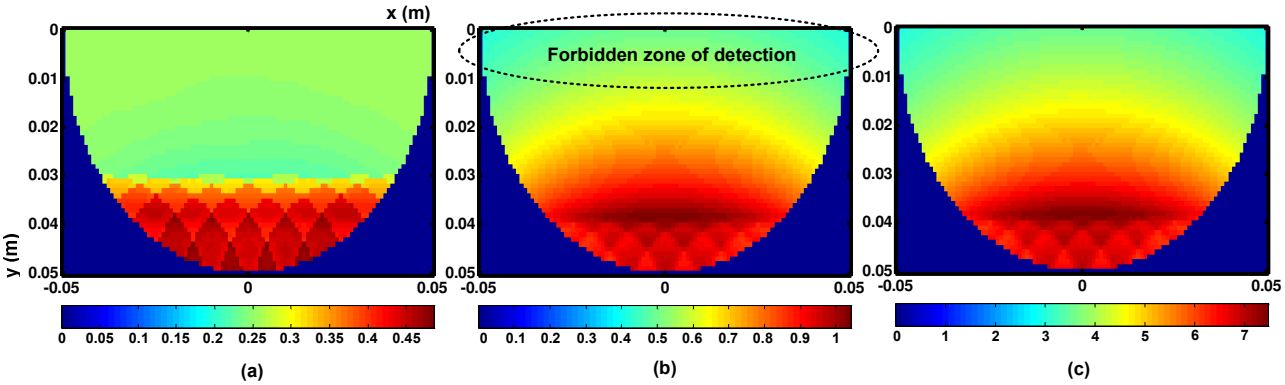

Fig. 5. (a) Mean clutter response (MCR) image, (b) clean tumor response (CTR) image, and (c) worst-case clutter response (WCR) image.

$$P_{\mathrm{WCR}}(\mathbf{r}_c) = \sum_{i=1}^{I}\left\{(N-1)\int_{\Xi_i} E\left(\tilde{\tau}_i(\mathbf{r}_c)\right)h^2(t)\,dt\right\} \qquad (11)$$

This parameter gives the maximum clutter response at any $\mathbf{r}_c$.

III. Numerical Examples

The geometry that generates synthetic data for our numerical examples is shown in Fig. 3. The imaging system is comprised of an array of 9 elements located at 1 cm from the top of the breast. We consider a dense breast tissue composition in the examples. The average dielectric properties of normal breast tissue are ε_b = 21.50 and σ_b = 1.66 S/m [4]. A number of 4-mm-diameter clutter sources are uniformly distributed in the breast phantom with a density of 1 cm^{-2}. These sources represent heterogeneous tissue and have an average dielectric-property-variation of 30%. The tumor (ε_t = 50.73 and σ_t = 4.82 S/m) is 2 mm in diameter. It is further assumed that the backscatter signal can be modeled as a 1st-order MHP with T = 14 ps (see also Fig. 4), and the integration window is 160 ps.

Fig. 5 depicts the detection images for the specified breast and signal models. A number of observations can be made from the figure. First, Fig. 5(a) shows that, generally, strong clutter responses are expected at the upper layer of the breast ($y \geq 0.03$ m), below which the MCR drops abruptly and shows little variation. However, for the CTR and WCR images shown in Fig. 5(b) and Fig. 5(c), the intensity value decreases smoothly as the focus point becomes farther away from the breast surface. Second, comparing Fig. 5(a) and Fig. 5(b) illustrates that there is a forbidden zone of detection for the current parameter setting. This region indicates the tumor locations where the CTR would be possibly comparable or even weaker than the MCR at the

performance measures have been proposed to evaluate the feasibilities of an imaging system for specified tissue compositions and UWB pulses. Finally, numerical examples have been presented to demonstrate the usefulness of these measures. A number of issues that need to be addressed in the future include: (i) extension of the generalized model to three-dimensional phantoms; (ii) extension of the analysis to realistic breast tissue structures for which double or multiple scatterings may occur; (iii) verification of the predicted model results through extensive full-wave electromagnetic simulations.

References

[1] D. Li, P. M. Meaney, and K. D. Paulsen, "Conformal microwave imaging for breast cancer detection," *IEEE Trans. Microw. Theory Tech.,* vol. 51, pp. 1179-1186, 2003.

[2] E. C. Fear, X. Li, S. C. Hagness, and M. A. Stuchly, "Confocal microwave imaging for breast tumor detection: Localization of tumors in three dimensions," *IEEE Trans. Biomed. Eng.,* vol. 49, pp. 812-822, 2002.

[3] E. J. Bond, X. Li, S. C. Hagness, and B. D. Van Veen, "Microwave imaging via space-time beamforming for early detection of breast cancer," *IEEE Trans. Antennas Propagat.,* vol. 51, pp. 1690-1705, 2003.

[4] S. K. Davis, H. Tandradinata, S. C. Hagness, and B. D. Van Veen, "Ultrawideband microwave breast cancer detection: A detection-theoretic approach using the generalized likelihood ratio test," *IEEE Trans. Biomed. Eng.,* vol. 52, pp. 1237-1250, 2005.

[5] Y. Chen, E. Gunawan, Y. Kim, K. S. Low, and C. B. Soh., "UWB microwave imaging for breast cancer detection: Tumor/clutter identification using a time of arrival data fusion method," accepted for presentation in *IEEE APS/URSI/AMEREM Symposium 2006,* July 2006.

[6] J. D. Taylor, *Introduction to Ultra-Wideband Radar Systems* CRC Press, Boca Raton, FL, 1995.

[7] M. Ghavami, L. B. Michael, S. Haruyama, and R. Kohno, "A novel UWB pulse shape modulation system," *Kluwer Wireless Personal Communications,* vol. 23, pp. 105-120, 2002.